Coupled lipidomics and digital pathology as an effective strategy to identify novel adverse outcome pathways in Eisenia fetida exposed to MoS2 nanosheets and ionic Mo

Sun, K.; White, J.C.; Qiu, H.; Gestel, C.A.M. van; Peijnenburg, W.J.G.M.; He, E.

Environmental Science & Technology

pubs.acs.org/est

Article

Coupled Lipidomics and Digital Pathology as an Effective Strategy to Identify Novel Adverse Outcome Pathways in *Eisenia fetida* Exposed to MoS_2 Nanosheets and Ionic Mo

Kailun Sun, Jason C. White, Hao Qiu,* Cornelis A. M. van Gestel, Willie J. G. M. Peijnenburg, and Erkai He*

Cite This: *Environ. Sci. Technol.* 2023, 57, 11009−11021

Read Online

ABSTRACT: Molybdenum disulfide (MoS_2) nanosheets are increasingly applied in several fields, but effective and accurate strategies to fully characterize potential risks to soil ecosystems are lacking. We introduce a coelomocyte-based *in vivo* exposure strategy to identify novel adverse outcome pathways (AOPs) and molecular endpoints from nontransformed ($NTMoS_2$) and ultraviolet-transformed ($UTMoS_2$) MoS_2 nanosheets (10 and 100 mg Mo/L) on the earthworm *Eisenia fetida* using nontargeted lipidomics integrated with transcriptomics. Machine learning-based digital pathology analysis coupled with phenotypic monitoring was further used to establish the correlation between lipid profiling and whole organism effects. As an ionic control, Na_2MoO_4 exposure significantly reduced (61.2−79.5%) the cellular contents of membrane-associated lipids (glycerophospholipids) in earthworm coelomocytes. Downregulation of the unsaturated fatty acid synthesis pathway and leakage of lactate dehydrogenase (LDH) verified the Na_2MoO_4-induced membrane stress. Compared to conventional molybdate, $NTMoS_2$ inhibited genes related to transmembrane transport and caused the differential upregulation of phospholipid content. Unlike $NTMoS_2$, $UTMoS_2$ specifically upregulated the glyceride metabolism (10.3−179%) and lipid peroxidation degree (50.4−69.4%). Consequently, lipolytic pathways were activated to compensate for the potential energy deprivation. With pathology image quantification, we report that $UTMoS_2$ caused more severe epithelial damage and intestinal steatosis than $NTMoS_2$, which is attributed to the edge effect and higher Mo release upon UV irradiation. Our results reveal differential AOPs involving soil sentinel organisms exposed to different Mo forms, demonstrating the potential of liposome analysis to identify novel AOPs and furthermore accurate soil risk assessment strategies for emerging contaminants.

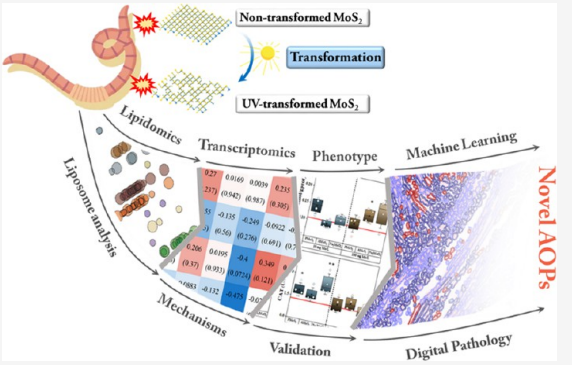

KEYWORDS: *MoS_2 nanosheets, ultraviolet irradiation, ecological risk, liposomes, coelomocyte, multi-omics, molecular mechanisms*

INTRODUCTION

Two-dimensional molybdenum disulfide nanomaterials (MoS_2 nanosheets) possess attractive electronic and mechanical properties that enable their application in numerous fields, including energy storage, biomedicine, and environment monitoring.[1−4] During their life cycle of production, use, and disposal, MoS_2 nanosheets will inevitably be released into the environment.[5] There is an increasing interest in assessing the environmental risk of MoS_2 nanosheets to ensure their safe and sustainable applications. However, the majority of existing work on MoS_2 nanosheet risk assessment has focused only on single-cell organisms or *in vitro* cell lines under relatively narrow exposure conditions;[6−8] effort is needed to develop rapid and accurate risk assessment frameworks based on important ecological sentinel species.

Soil ecosystems are an important sink for environmental contaminants such as MoS_2 nanomaterials. As ecological engineers, earthworm species are sensitive and widespread soil invertebrates.[9] Coelomocytes are free-flowing immune cells in the earthworm that play a key role in the phagocytosis and digestion of xenobiotics.[10,11] Recently, *in vitro* exposure strategies based on earthworm coelomocytes have been developed to shorten the exposure period and reduce animal consumption.[12,13] Although coelomocytes are considered a suitable system for cellular-level testing, the simplified *ex vivo* exposure environment lacks the overall response conditions of the organism and therefore cannot reflect the *in vivo* biological response of realistic exposure scenarios. Importantly, the risk assessment based on soil fauna still has been limited by the

Received: April 4, 2023
Revised: May 24, 2023
Accepted: July 3, 2023
Published: July 20, 2023

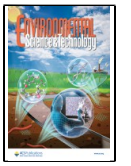

https://doi.org/10.1021/acs.est.3c02518
Environ. Sci. Technol. 2023, 57, 11009−11021

scarcity of biomarkers and the low sensitivity of adverse outcome detection, thus lacking in effectiveness and accuracy. Accordingly, it is highly desirable to develop a more accurate and efficient risk assessment strategy that combines the advantages of high sensitivity, rapid turnaround time, and animal friendliness, facilitating identifying novel adverse outcome pathways (AOPs) for contaminants such as MoS_2 nanosheets in soil sentinel organisms.

Liposomes are involved in a wide range of biological functions that are jointly regulated as part of a range of complex interconnected physiological networks.[14] Many of these sensitive biological processes may be affected by exposure to environmental pollutants. The recent development of mass spectrometry-enabled identification of complex liposomes in tissues and cells has further expanded the ability to screen for diseases and enabled the development of related biomarkers.[15] For example, Sun et al. successfully identified a food antioxidant (3-BHA) that exacerbated the development of nonalcoholic fatty liver disease from high-fat diets by disrupting hepatic lipid homeostasis.[16] Lipidomics also helped to reveal the link between lipid changes and Parkinson's disease, malignancies, liver lesions, and abnormal spleen metabolism.[17−21] Marqueño et al. and Zhen et al. used lipidomics to characterize the effects of complex contaminated water bodies on liposomal changes of skeletal muscle in *Barbus meridionalis* and *Squalius laietanus*, as well as liver cells in *Danio rerio*.[14,22] Monitoring of complex liposomes has demonstrated advantages in globally characterizing unpredictable adverse effects and has forwarded efforts to develop critical biomarkers (membrane homeostasis, oxidative stress, mitochondrial disorders, etc.) in organisms under environmental stress. The integration of multi-omics strategies offers the opportunity to further relate lipid profiling and molecular effects to mechanistically understand impacts on higher levels of biological organization. Considering the vast biocomplexity of liposomes and the analytical power of mass spectrometry-based tools, we are sought to establish a risk assessment framework based on nontargeted lipidomics to elucidate novel AOPs and molecular mechanisms of MoS_2 nanosheets to an environmental sentinel species.

Recent work has demonstrated that MoS_2 nanosheets are susceptible to transformation (e.g., morphological and size changes, ion species release, etc.) upon engineered modification or environmental aging processes.[5,23−27] Importantly, compared to the nontransformed form, the biological effects of the transformed MoS_2 nanosheets on sensitive biota may be significantly different.[5,6,24,28] Ultraviolet (UV) is a commonly used engineering modification technique and an important environmental aging factor. UV irradiation can readily oxidize the crystal substrate of MoS_2 nanosheets, leading to phase transitions and surface defects that accelerate structural fragmentation.[29] Shi et al. reported the generation of nanopores on the basal plane of MoS_2 nanosheets induced by simulated UV irradiation.[27] Cao et al. observed nanoscale stripes on the surface of MoS_2 nanosheets with enhanced hydrophilicity and a greater friction coefficient following UV/ozone aging.[29] Although studies have shown that UV irradiation can significantly affect the lattice structure and physicochemical properties of MoS_2 nanosheets, the role of such transformations in the risk profile of MoS_2 nanosheets is poorly understood.

We developed a coelomocyte-based *in vivo* exposure strategy to achieve accurate and rapid risk assessment of MoS_2 nanosheets to earthworms (*Eisenia fetida*). It was assumed that *in vivo* exposure to MoS_2 nanosheets (nontransformed and UV-transformed) and their ionic counterpart (Na_2MoO_4) would alter the liposome profiling of earthworm coelomocytes in distinguishable patterns and mechanisms. To test this hypothesis, earthworm coelomocytes were isolated through a noninvasive method for the orthogonal liposome−transcriptome−phenotype analysis. Nontargeted lipidomics integrated with transcriptomics was performed to understand the lipid-related AOPs and upstream molecular mechanisms in an unbiased and mechanistic fashion. The lipidomic results were validated using machine learning-based histopathological examination and associated phenotypic monitoring. This work will expand our understanding of the potential of liposome analysis in identifying novel AOPs and enabling the development of more accurate and efficient frameworks for soil ecological risk assessment.

MATERIALS AND METHODS

Synthesis of UV-Transformed MoS_2 Nanosheets. In this study, MoS_2 nanosheets were chemically exfoliated at XFNANO Materials Tech. Co., Ltd., Jiangsu, China, as detailed in Text S1. The exfoliated nontransformed MoS_2 nanosheets ($NTMoS_2$, 1 mg/mL) were continuously irradiated using a 500 W mercury lamp (200−400 nm, with a main wavelength peak at 365 nm) for 12 h at 25 °C under magnetic stirring. The irradiation wavelength and time follow the environmental conditions and commonly reported parameters for engineered modification. UV-transformed MoS_2 nanosheets ($UTMoS_2$) were collected by filtration through 0.1 μm polyether sulfone membranes and freeze-dried for 48 h. Sodium molybdate (Na_2MoO_4, >99%) was selected as an ionic control in this study. Two forms of MoS_2 nanosheets were characterized as described in Text S1. Details of the tested organisms and reagents used in this study are given in Text S2.

***In Vivo* Earthworm Exposure Strategy and Isolation of Coelomocytes.** In this study, the homogenized agar recommended by Organization for Economic Co-operation and Development (OECD) and International Organization for Standards (ISO) was used as the exposure medium to allow identification of the effects and associated toxicity mechanisms of MoS_2 nanosheets on *E. fetida*.[30,31] This exposure medium can exclude additional damage to the earthworm body wall and gut from soil particle friction or ingestion and minimizes the uncontrolled *ex vivo* transformation of MoS_2 nanosheets. The representative exposure concentrations selected in this study were determined by the literature survey and the prediction of environmentally relevant concentrations of MoS_2 nanosheets, meeting the range of soil biological tolerances (Text S3 and Table S1). Seven treatments were established: (1) clean agar as control; (2) agar with a low dose (10 mg Mo/L) of $NTMoS_2$ ($NTMoS_2$-L); (3) agar with a high dose (100 mg Mo/L) of $NTMoS_2$ ($NTMoS_2$-H); (4) agar with a low dose (10 mg Mo/L) of UV-transformed MoS_2 ($UTMoS_2$-L); (5) agar with a high dose (100 mg Mo/L) of UV-transformed MoS_2 ($UTMoS_2$-H); (6) agar with a low dose (10 mg Mo/L) of Na_2MoO_4 (Na_2MoO_4-L); and (7) agar with a high dose (100 mg Mo/L) of Na_2MoO_4. Each treatment level contained six independent biological replicates. After domestication and 24 h of depuration, adult earthworms with clearly visible clitellum were transferred to the medium and exposed continuously for 96 h in a greenhouse at 25 ± 1 °C. The coelomocytes were

https://doi.org/10.1021/acs.est.3c02518
Environ. Sci. Technol. 2023, 57, 11009−11021

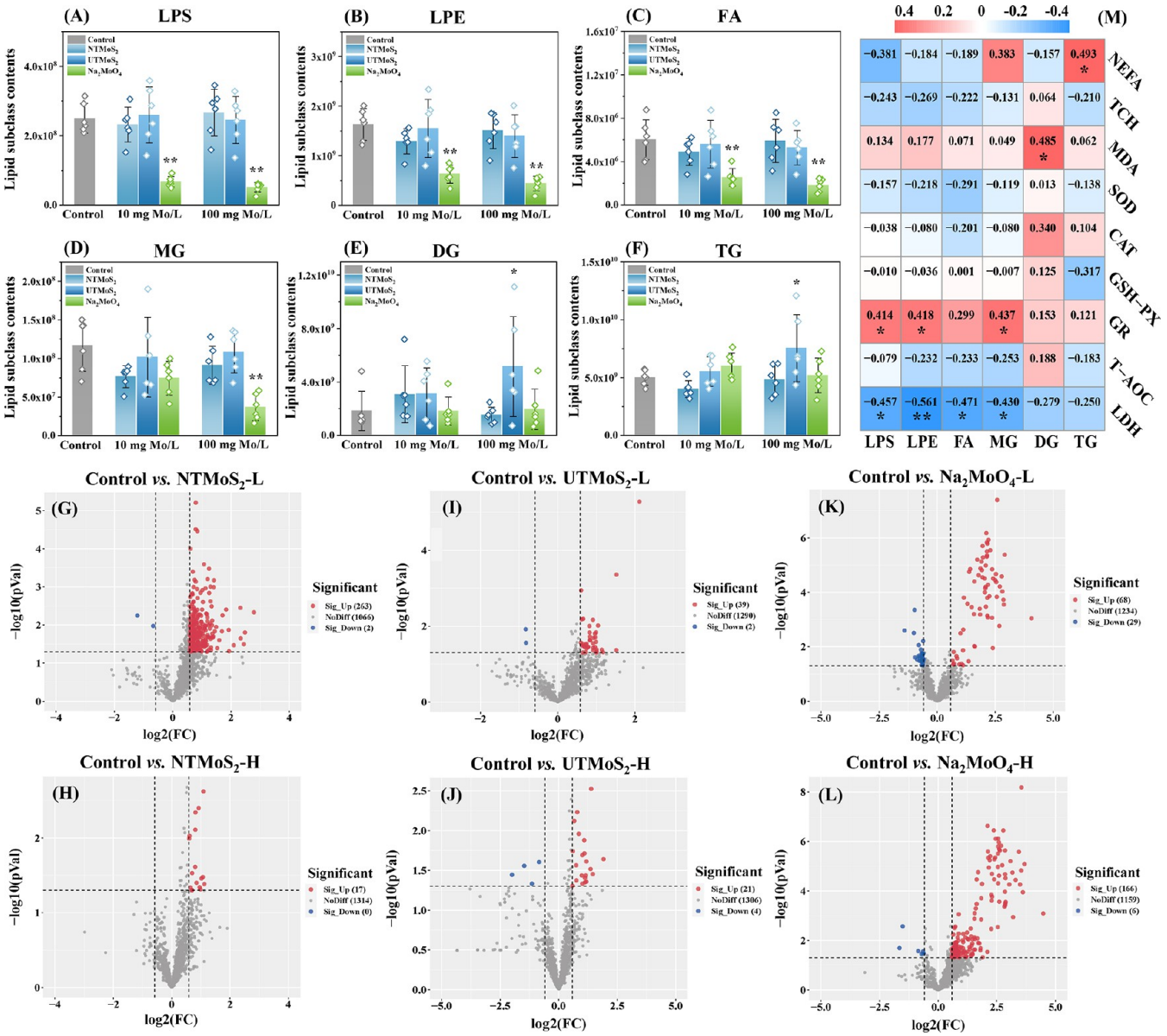

Figure 1. Nontargeted lipidomic profiles of earthworm (*E. fetida*) coelomocytes following *in vivo* exposure for 96 h to different Mo forms (nontransformed ($NTMoS_2$) and UV-transformed ($UTMoS_2$) MoS_2 nanosheets) and Na_2MoO_4 at two concentrations (L: 10 mg Mo/L; H: 100 mg Mo/L). (A–F) Six critical and significantly changed lipid subclasses across different treatments ($p < 0.05$). The content of lipid subclasses was expressed as the chromatographic peak intensity. (G–L) Visualized volcano maps of detected lipid species from different comparisons. The thresholds of *p*-value and fold change for differential lipid species (DLSs) were set at 0.05 and 1.5. (M) Correlation analysis between lipidomics (at the subclass level) and phenotypic results. Numbers represent correlation coefficients. Statistically significant differences compared to the control are expressed as $*p < 0.05$ and $**p < 0.01$.

isolated using a noninvasive method after 24 h of earthworm depuration (details are given in Text S4).[32]

Lipidomics Analysis. Cellular lipids were extracted by the methyl *tert*-butyl ether (MTBE) method. Briefly, 30 mg of cell deposit was mixed with 200 μL of ultrapure water and vortexed vigorously for 5 s. Subsequently, 240 μL of precooled methanol and 800 μL of MTBE were added. The mixed solution was centrifuged at 14 000 rpm for 15 min at 10 °C to obtain the upper organic solvent layer, which was dried under nitrogen. The obtained lipid extracts were redissolved in 200 μL of 90% isopropanol/acetonitrile, centrifuged at 14 000 rpm for 15 min, and the supernatant was used for liquid chromatography coupled to tandem mass spectrometry analysis (LC-MS/MS; detailed in Text S5). The stability and reliability of instrumental analysis and lipidomics data were demonstrated through quality control (QC) samples prepared by mixing equal amounts of tested samples (Figure S1 and Text S6).

RNA Sequencing. Cellular RNA was extracted using a TRIZOL reagent according to the manufacturer's protocol. The purity and integrity of extracted RNA were assessed by Nanodrop 2000 and agarose gel electrophoresis, respectively. Samples with satisfactory RNA quality were sequenced on an Illumina Novaseq. 6000 sequencing platform, followed by library construction via the Illumina Truseq RNA sample prep Kit method. More details of the RNA sequencing are shown in Text S7.

https://doi.org/10.1021/acs.est.3c02518
Environ. Sci. Technol. 2023, 57, 11009−11021

Detection of Liposome-Related Phenotypic Changes in Earthworm Coelomocytes. After *in vivo* exposure, isolated coelomocytes were resuspended in 0.8 mL of saline (0.85%) and cell homogenates were prepared by high-speed grinding. Following the manufacturer's protocol, several commercial kits (Nanjing Jiancheng Bioengineering Institute, Nanjing, China) were used to detect cellular superoxide dismutase (SOD), catalase (CAT), glutathione peroxidase (GSH-PX), glutathione reductase (GR) activities, total antioxidant capacity (T-AOC), malondialdehyde (MDA), and lactate dehydrogenase (LDH) contents to assess intracellular redox status and membrane integrity. The nonesterified fatty acid (NEFA) and total cholesterol (TCH) contents were measured to assess intracellular lipid levels. The detailed assay steps and the enzyme unit activity definitions are listed in Tables S2−S10.

Microstructure Observation and Quantification of Mo Content of Earthworm. After *in vivo* exposure, the earthworms were transferred to 4% paraformaldehyde and fixed for 48 h. At room temperature, the earthworms were cut into 3 μm sections and embedded in paraffin. The sections were stained using hematoxylin−eosin (HE), and images were obtained under a microscope. Subsequently, an open-source image analysis platform, Qupath, was applied to perform deep learning, automated quantification, and objective screening for pathological images (detailed in Text S8).[33] Quantification of the Mo content in earthworm tissue was performed according to our previously established method,[34] as detailed in Text S9.

Statistical Analysis. The statistical differences between groups were analyzed (one-way ANOVA or *t*-test) by GraphPad Prism (V. 7.0). For lipidomics and transcriptomics, bioinformatics analysis methods are detailed in Text S10.

RESULTS AND DISCUSSION

Characterization of Nontransformed ($NTMoS_2$) and UV-Transformed ($UTMoS_2$) MoS_2 Nanosheets. Transmission electron microscopy (TEM) images showed that the $NTMoS_2$ possesses a flat basal plane with inhomogeneous lateral dimensions (Figure S2A). UV irradiation resulted in dense nanopore formation on MoS_2 nanosheets (Figure S2B), with marginal changes in size ranges (Figure S3) and surface functional groups (Figure S4). The elevated specific surface area (Figure S5A; from 0.70 to14.29 cm^2/g) and the total pore volume (Figure S5B; from 0.0057 to 0.060 cm^3/g) from the Brunauer−Emmett−Teller (BET) analysis confirmed the porous morphology (pore size ∼5−15 nm; Figure S5C) of $UTMoS_2$. High-resolution TEM (HR-TEM) images showed that UV irradiation increased the lattice spacing of MoS_2 nanosheets (Figure S6; from 0.32 ± 0.02 to 0.39 ± 0.12 nm, $p < 0.05$) and explained the essence of nanopores as clustered atomic vacancies.[27] The detected higher release of Mo (MoO_4^{2-}, $p < 0.01$) and S species (SO_4^{2-}, $p < 0.05$) (Figure S7) supported the Mo and S atom oxidation of $UTMoS_2$.[3,25,26] The A_{1g} (∼405 cm^{-1}) to $E_{2g}{}^1$ (∼380 cm^{-1}) blue shifts of Raman peaks and higher $A_{1g}-E_{2g}{}^1$ ratio of $UTMoS_2$ (from 2.26 to 2.36) indicated the lattice distortion of MoS_2 nanosheets after UV irradiation (Figure S8),[35,36] which is further confirmed by the improved surface roughness (Figure S9; from 0.61 to 0.95). The above data indicate that UV-mediated oxidation and dissolution of Mo and S atoms on MoS_2 nanosheets are responsible for porous morphology formation. The nanopore structure possesses abundant edge sites and dangling bonds that may alter their biological effects.[27,37−39] This is verified in the following sections.

Nontargeted Lipidomics Reveals Common and Unique Lipid Profile Changes in Earthworm Coelomocytes. A total of 40 lipid subclasses, including 1331 lipid species, were identified across all 7 treatments, demonstrating a good detection breadth and depth. The composition of the lipid subclasses for each treatment is shown in Figure S10. Phosphatidylcholine (PC, 30.15−34.90%), phosphatidylinositol (PI, 13.34−17.44%), sulfatide (ST, 13.43−15.43%), and phosphatidylethanolamine (PE, 9.91−11.74%) were the dominant lipid subclasses but without significant lipid content or structural changes across the treatments. These results are consistent with the high percentage of PC, PE, PI, and ST in other eukaryotic cells.[40,41] Several lipids with lower relative abundance but are responsible for key biological functions deserve special attention, as their contents varied significantly (ANOVA) upon different treatments.

Lipid Subclasses Changes. Lipids typically perform physiological functions as subclass groups.[42] Six critical and significantly changed ($p < 0.05$) lipid subclasses are shown in Figure 1A−F. Compared to the control, the levels of the lipid subclasses lyso-phosphatidylserine (LPS), lyso-phosphatidylethanolamine (LPE), and fatty acid (FA) were significantly downregulated ($p < 0.01$) upon exposure to 10 and 100 mg Mo/L Na_2MoO_4, while no significant changes were observed in the two types of MoS_2 nanosheet-exposed groups (Figure 1A−C). LPS and LPE are two important subclasses of glycerophospholipids, which are the main structural components of cell membranes. Therefore, the metabolic inhibition of glycerophospholipids and FA suggests that Na_2MoO_4 may cause a partial loss of membrane stability.[43] This is supported by the significant decrease in unsaturation and carbon chain length of LPE and monoglyceride (MG) subclasses under Mo ion exposure (Figures S11 and S12). There is evidence that the homeostasis of glycerophospholipids is closely related to the dynamic changes of glycerides.[16] The content of MG, a subclass of glycerides, decreased significantly ($p < 0.01$) upon exposure to 100 mg Mo/L of Na_2MoO_4 (Figure 1D), indicating that glyceride metabolism was inhibited by Mo ions. In addition to MG, following *in vivo* exposure to 100 mg Mo/L of $UTMoS_2$, the diglyceride (DG) level in earthworm coelomocytes was significantly upregulated by 179% compared to that of the control (Figure 1E, $p < 0.05$). Meanwhile, $UTMoS_2$ exposure resulted in a significant upregulation (50.6%, $p < 0.05$) of triglyceride (TG) levels in the high-concentration group (Figure 1F), while the $NTMoS_2$ and Na_2MoO_4 exposure groups showed no such changes. These results suggest that 100 mg Mo/L of $UTMoS_2$ specifically induced the hypermetabolism of glycerides (including DG and TG). One possible mechanism is that nanopores provide potential active sites and exposed bonds that alter the coelomocyte lipid metabolism pattern by facilitating the electron transport between the MoS_2 nanosheets and cell membrane.[27,39] The contents of phospholipids (PC, PE, and PI) and ST subclasses did not change significantly among the different exposures, although a higher relative abundance was evident (Table S11). Furthermore, both doses of $NTMoS_2$ and $UTMoS_2$ not only significantly decreased the unsaturation degree and the carbon chain length of the zymosterol (ZyE) subclass but also caused an increase in the carbon chain length of the DG subclass (Figures S11 and S12). Taken together, Na_2MoO_4 significantly inhibited the synthesis of liposomes

https://doi.org/10.1021/acs.est.3c02518
Environ. Sci. Technol. 2023, 57, 11009−11021

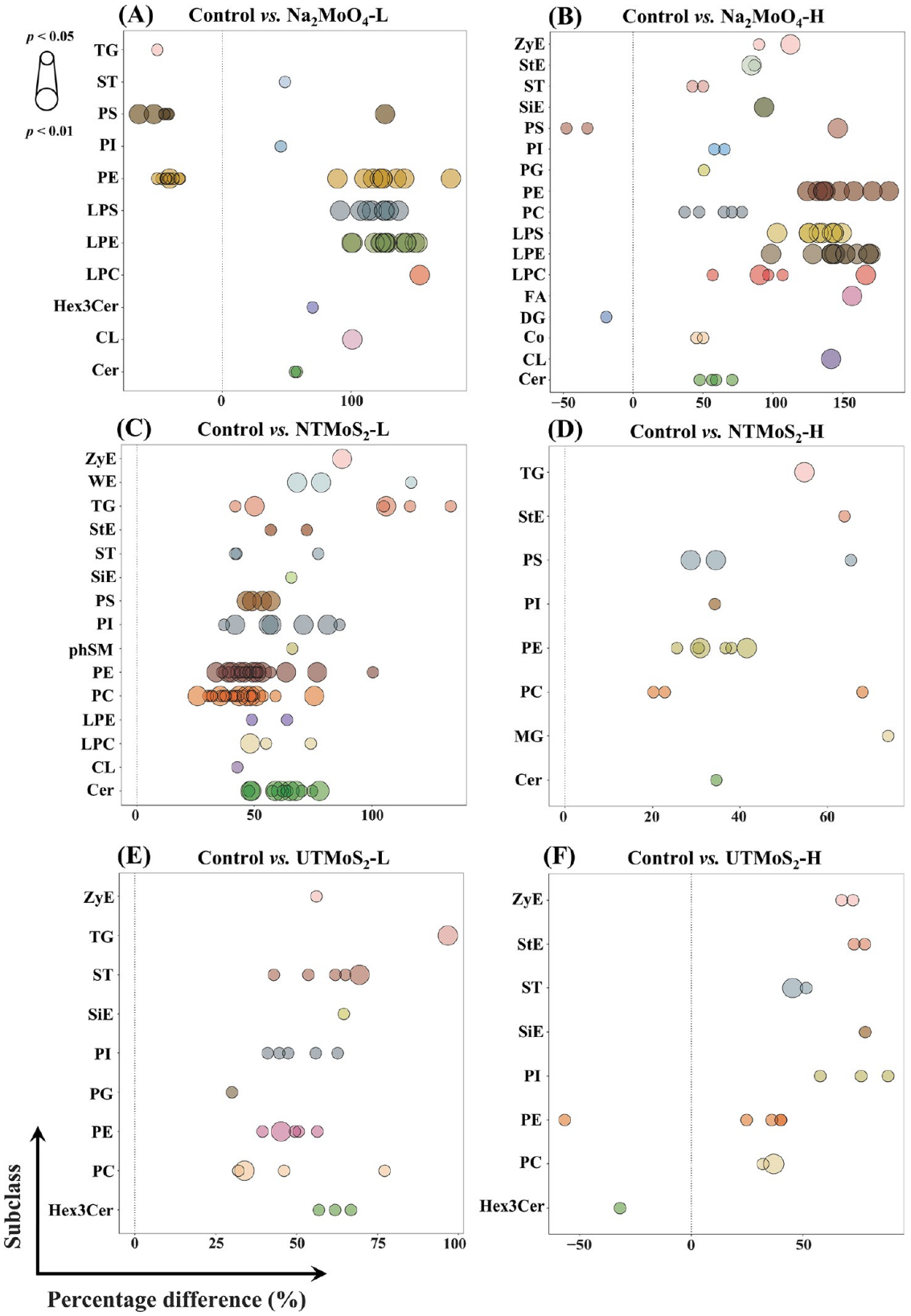

Figure 2. Bubble maps of differential lipid species (VIP > 1.0 and $p < 0.05$) in earthworm (*E. fetida*) coelomocytes *in vivo* exposed for 96 h to (A, B) Na_2MoO_4 and (C, D) nontransformed ($NTMoS_2$) and (E, F) UV-transformed ($UTMoS_2$) MoS_2 nanosheets at two concentrations (L: 10 mg Mo/L; H: 100 mg Mo/L).

involved in membrane homeostasis and reduced the unsaturation degree and carbon chain length of related lipid subclasses. Compared to ionic molybdate, $NTMoS_2$ had no significant effect on lipid subclass content, whereas 100 mg Mo/L of $UTMoS_2$ induced glyceride hypermetabolism.

https://doi.org/10.1021/acs.est.3c02518
Environ. Sci. Technol. 2023, 57, 11009−11021

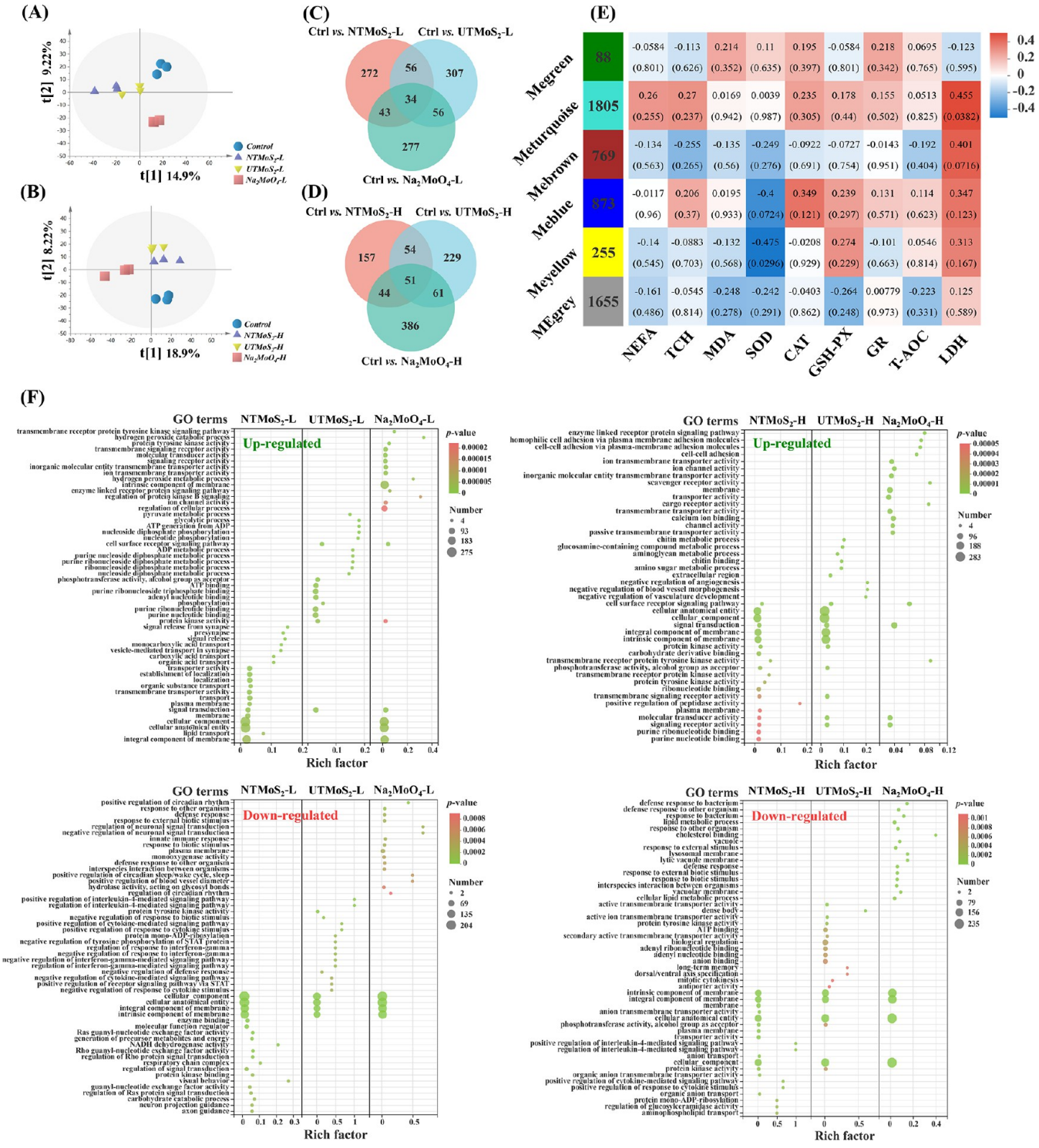

Figure 3. Transcriptomics changes of lipid-related target genes in earthworm (*E. fetida*) coelomocytes *in vivo* exposed for 96 h to nontransformed ($NTMoS_2$) and UV-transformed ($UTMoS_2$) MoS_2 nanosheets and Na_2MoO_4. (A, B) PLS-DA and (C, D) Venn diagram analysis performed on 10 mg Mo/L (L) and 100 mg Mo/L (H) exposure groups. WGCNA analysis (E) was used to correlate transcriptomics and phenotypic results. Numbers represent correlation coefficients and *p*-values (in parentheses). (F) GO enrichment analysis ($p < 0.05$).

Lipid Species Perturbation. Partial least-squares discriminant analysis (PLS-DA) was performed on identified 1331 lipid species to investigate intergroup differences. The data from Na_2MoO_4 exposures were separated from the other groups at both doses, indicating that molybdate caused more significant overall lipid species level perturbation (Figure S13A,B). When molybdate was excluded, $NTMoS_2$ and $UTMoS_2$ disturbed the lipid metabolism of earthworm coelomocytes differently (Figure S13C,D). Visualized volcano plots clearly show that far more differential lipid species (DLSs) were upregulated than downregulated upon all exposures (Figure 1G–L), suggesting a lipid hypermetabolism in coelomocytes exposed *in vivo* to two types of MoS_2 nanosheets and Na_2MoO_4. Molybdate exposure induced a

https://doi.org/10.1021/acs.est.3c02518
Environ. Sci. Technol. 2023, 57, 11009−11021

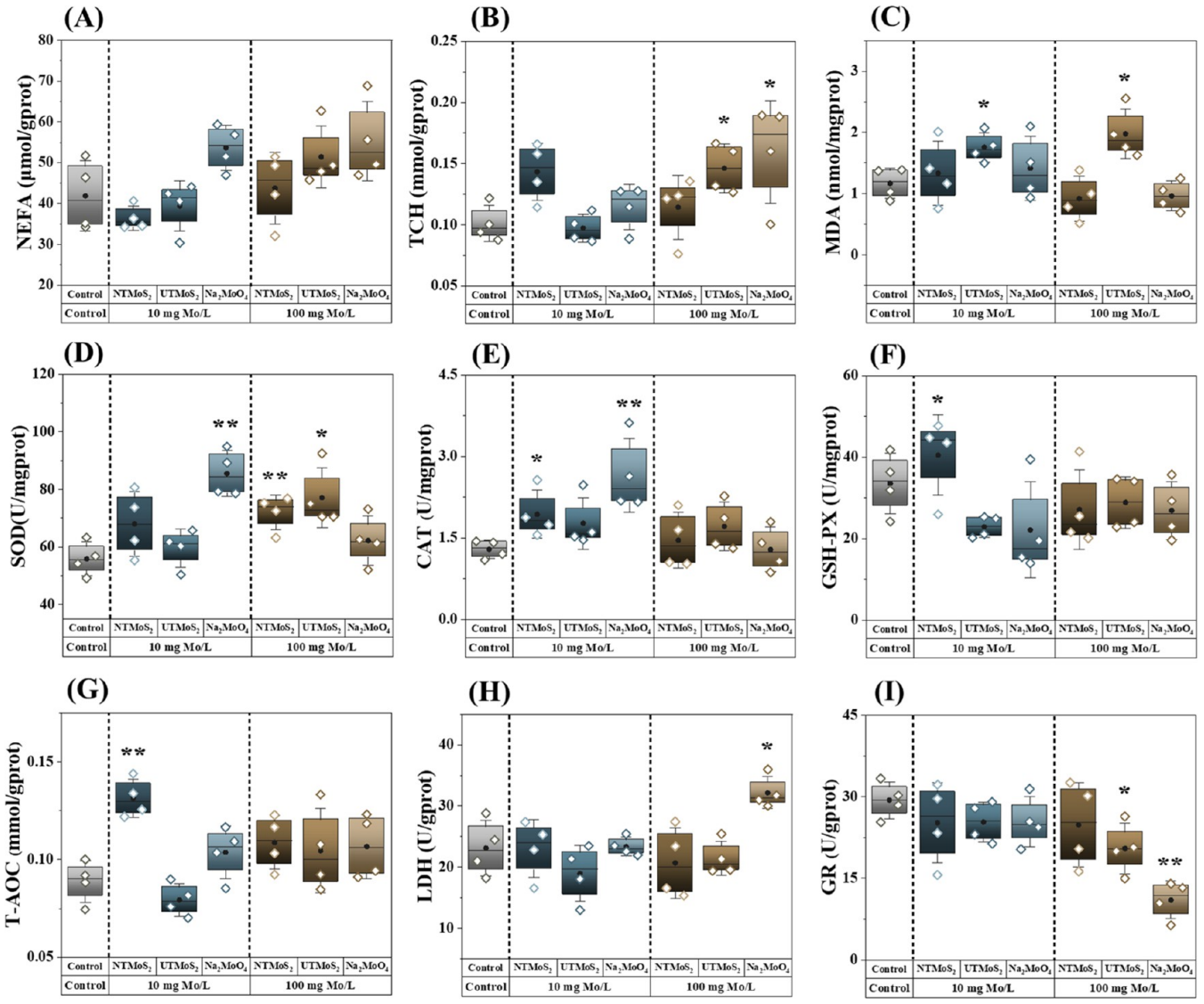

Figure 4. (A) NEFA and (B) TCH contents in earthworm (*E. fetida*) coelomocytes *in vivo* exposed to two concentrations (10 and 100 mg Mo/L) of nontransformed ($NTMoS_2$) and UV-transformed ($UTMoS_2$) MoS_2 nanosheets and Na_2MoO_4 in an agar medium. Coelomocyte redox and membrane homeostasis were characterized by (C) MDA contents, (D) SOD activities, (E) CAT activities, (F) GSH-PX activities, (G) T-AOC levels, (H) LDH contents, and (I) GR activities. The top and bottom boundaries of the boxes show the 25th and 75th percentiles, respectively; the mean and median of the data are marked as black dots and horizontal lines in the boxes, respectively. Statistically significant differences compared to the control are expressed as $*p < 0.05$ and $**p < 0.01$.

more pronounced lipid species disorder than the two types of MoS_2 nanosheets, and the control and MoS_2 nanosheet exposures were clustered in the same hierarchy under the positive ion mode (Figure S14A). These findings are consistent with the obvious differences from Na_2MoO_4 in PLS-DA score plots (Figure S13A,B). Significant ionic group separation was also observed in the negative ion mode, but the effects of $NTMoS_2$ and $UTMoS_2$ on coelomocyte liposomes were similar (Figure S14B). The subclass distribution of DLSs was further identified (Figure 2). The DLSs in coelomocytes exposed to Na_2MoO_4 (10 and 100 mg Mo/L) were distributed among PE, lysophosphatidylcholine (LPC), and LPS subclasses (Figure 2A,B). It has been demonstrated that LPS and LPE transformed from PC are directly associated with cell membrane damage.[44,45] Unlike molybdate, the coelomocyte DLSs upon $NTMoS_2$ exposure were primarily phospholipids, including phosphatidylserine (PS), PI, PE, and PC (Figure 2C,D). This implies a positive membrane structure remodeling of coelomocytes under $NTMoS_2$ stress.[16] $UTMoS_2$ exposure resulted in the differential upregulation of ST (Figure 2E,F), which may be associated with the cellular response to $UTMoS_2$-induced energy deprivation as ST plays a critical role in cellular signal transduction and energy homeostasis processes.[46]

Lipid-Associated Transcriptomics Further Probe the Molecular Initiation Events. Transcriptomics was used to further reveal and predict the molecular initiating events of lipid disorders. PLS-DA performed on all screened lipid-related genes clearly distinguished gene expression differences between $NTMoS_2$, $UTMoS_2$, Na_2MoO_4, and control groups (Figure 3A,B). The 10 and 100 mg Mo/L groups were also well separated (Figure S15). The Venn diagram analysis confirmed the difference in concentration, as differentially expressed genes (DEGs) shared in 10 and 100 mg Mo/L

https://doi.org/10.1021/acs.est.3c02518
Environ. Sci. Technol. 2023, 57, 11009−11021

groups only accounted for 10.9, 11.4, and 14.4% of the total DEGs, respectively (Figure S16). Visual analysis based on volcano plots showed that more genes were significantly upregulated than downregulated at all doses (Figure S17). With increasing dose, fewer genes were upregulated and more genes were downregulated in $NTMoS_2$ and $UTMoS_2$ groups, while the opposite pattern was observed upon Na_2MoO_4 exposure. Hierarchical clustering (HCL) analysis further revealed that Na_2MoO_4 caused more significant changes in gene expression than MoS_2 nanosheets at 10 mg Mo/L (Figure S18A). The gene expression pattern of coelomocytes with $UTMoS_2$ was similar to that of Na_2MoO_4 at 100 mg Mo/L (Figure S18B). The Venn diagram analysis based on all treatments showed that 34 and 51 DEGs were coregulated by $NTMoS_2$, $UTMoS_2$, and Na_2MoO_4 at 10 and 100 mg Mo/L, respectively (Figure 3C,D).

A weighted coexpression network analysis (WGCNA) was applied to correlate unigenes regulating lipid homeostasis with evidence of phenotypic alterations. All target unigenes were divided into 6 modules (Figure 3E). Unigenes in the Meturquoise module were significantly positively correlated with LDH activity ($R = 0.455$, $p = 0.0382$), while those in the Meyellow module were significantly negatively correlated with SOD activity ($R = -0.475$, $p = 0.0296$). Gene Ontology (GO) enrichment results for unigenes in each of these two modules validated the correlation analysis results, as unigenes in the Meturquoise module play important roles in regulating membrane homeostatic processes, while unigenes in the Meyellow module closely regulate cellular stress response and transmembrane receptor activity (Figure S19).

Next, all DEGs were matched in the GO and Kyoto Encyclopedia of Genes and Genomes (KEGG) databases. Na_2MoO_4 exposure at 10 mg Mo/L resulted in an upregulation of DEGs associated with H_2O_2 catabolism (Figure 3F), which is consistent with the significant increase ($p < 0.01$) in CAT activity at this concentration (Figure 4E). The downregulated DEGs in the Na_2MoO_4 group were significantly enriched in the categories of steroid and unsaturated fatty acid biosynthesis (Figure S20). Inhibition of sterol and unsaturated fatty acid *de novo* synthesis by Na_2MoO_4 could lead to energy deprivation.[46] This is confirmed by the significant enrichment of the riboflavin metabolic pathway (Figure S20), which plays a key role in energy production.[47] In addition, the downregulated immune response pathway suggests the presence of immune stress caused by Na_2MoO_4 exposure (Figure 3F).

Compared to Na_2MoO_4, $NTMoS_2$ inhibited the expression of genes related to ion transport across membranes, which may counteract Mo ion damage by actively regulating osmotic pressure and cellular ion uptake.[48] The lipidomics analysis supports this hypothesis, as $NTMoS_2$-upregulated DLSs were significantly enriched in the glycerophospholipids (PS, PI, PE, PC) (Figure 2C,D). Glycerophospholipids are major structural components of cell membranes and are involved in membrane homeostasis by providing precursors for signaling molecules.[49] Additionally, downregulated DEGs significantly correlated with oxidative phosphorylation and glycolysis (Figure S20), which is indicative of stress on cellular energy homeostasis.[50,51]

Unlike $NTMoS_2$, genes involved in lipolysis were activated upon exposure to $UTMoS_2$ at 10 mg Mo/L (Figures 3F and S20). Consistent with the differential upregulation of lipid subclass ST related to energy homeostasis in lipidomics, these results suggest a positive cellular response to compensate for $UTMoS_2$-induced energy deprivation. $UTMoS_2$ at 100 mg Mo/L activated the apoptotic pathway. Apoptosis is typically accompanied by the loss of membrane homeostasis.[52] Given the significant impact of Na_2MoO_4 on the membrane structure and its associated lipids, the role of ionic Mo release in $UTMoS_2$-induced lipid disorders deserves attention.

Phenotypic Consequences Verified the Liposome Disorder in Coelomocytes. Dysregulation of liposomes may have a range of adverse consequences, including energy destabilization and lipid peroxidation.[53,54] The content of NEFA in earthworm coelomocytes upon *in vivo* exposure to Na_2MoO_4 increased in a dose-dependent fashion up to 31.9% of the controls (n.s., Figure 4A). Two types of MoS_2 nanosheets at 100 mg Mo/L also caused intracellular accumulation of NEFA (4.45%, 22.7%, n.s.). As a decomposition product of neutral fat, an elevated NEFA content is correlated with abnormal mitochondrial respiration.[55] The significant accumulation of intracellular TCH upon exposure to $UTMoS_2$ and Na_2MoO_4 at 100 mg Mo/L ($p < 0.05$; Figure 4B) confirms the $UTMoS_2$- and Na_2MoO_4-induced upregulation of DLSs in the ST subclass (Figure 2).

Given the observed lipid dysregulation, we speculate that hypermetabolized liposomes, particularly polyunsaturated fatty acids, could be rapidly and extensively peroxidized by reactive oxygen species (ROS). To test this hypothesis, we measured MDA levels, the end product of lipid peroxidation.[56] As expected, UV-transformed MoS_2 nanosheets induced significant lipid peroxidation (50.4−69.5%, $p < 0.05$; Figure 4C) in a dose-dependent fashion. The significant positive correlation between DG and MDA ($R = 0.485$, $p = 0.0162$; Figure 1M) further indicates that $UTMoS_2$-induced lipid peroxidation was closely related to glyceride hypermetabolism. The occurrence of lipid peroxidation is a function of the intracellular redox status.[57] $NTMoS_2$ at 100 mg Mo/L caused a significant elevation of SOD activity in the coelomocytes (Figure 4D; $p < 0.01$). Meanwhile, CAT, GSH-PX, and T-AOC were activated upon $NTMoS_2$ exposure at 10 mg Mo/L ($p < 0.05$; Figure 4E−G), suggesting the positive response of the coelomocyte antioxidant system to prevent lipid peroxidation.[58−60] Detection of LDH levels, a biomarker of cell membrane integrity,[7,27] confirmed the Na_2MoO_4-induced membrane stress as 100 mg Mo/L of Na_2MoO_4 caused significant LDH leakage ($p < 0.05$; Figure 4H). Compared to $NTMoS_2$, 100 mg Mo/L of $UTMoS_2$ and Na_2MoO_4 significantly inhibited the GR activity ($p < 0.05$; Figure 4I). Notably, correlation analysis showed that glycerophospholipids (LPS, LPE) and glyceride (mainly MG) were significantly and positively correlated with the GR activity (Figure 1M). GR is not involved in the direct scavenging of ROS but enables the function of GSH-PX.[61,62] Therefore, the inhibition of the GR activity by $UTMoS_2$ and Na_2MoO_4 may indirectly lead to the inability to scavenge ROS and subsequently mediate the loss of membrane homeostasis in conjunction with disturbed glycerophospholipid and glyceride metabolism.[43]

Accumulation of Mo from Different Mo Forms. Alterations in the liposomes and associated phenotypes in coelomocytes may be related to the accumulation of Mo from different Mo forms. The uptake (including oral ingestion and tissue absorption) of total Mo from different Mo forms at 10 mg Mo/L showed no significant difference compared to the control (Figure S21A). At 100 mg Mo/L, the total Mo concentrations in earthworms exposed to $NTMoS_2$, $UTMoS_2$, and Na_2MoO_4 were 24.6, 30.0, and 46.0 $\mu g/g$ (d.w.),

https://doi.org/10.1021/acs.est.3c02518
Environ. Sci. Technol. 2023, 57, 11009−11021

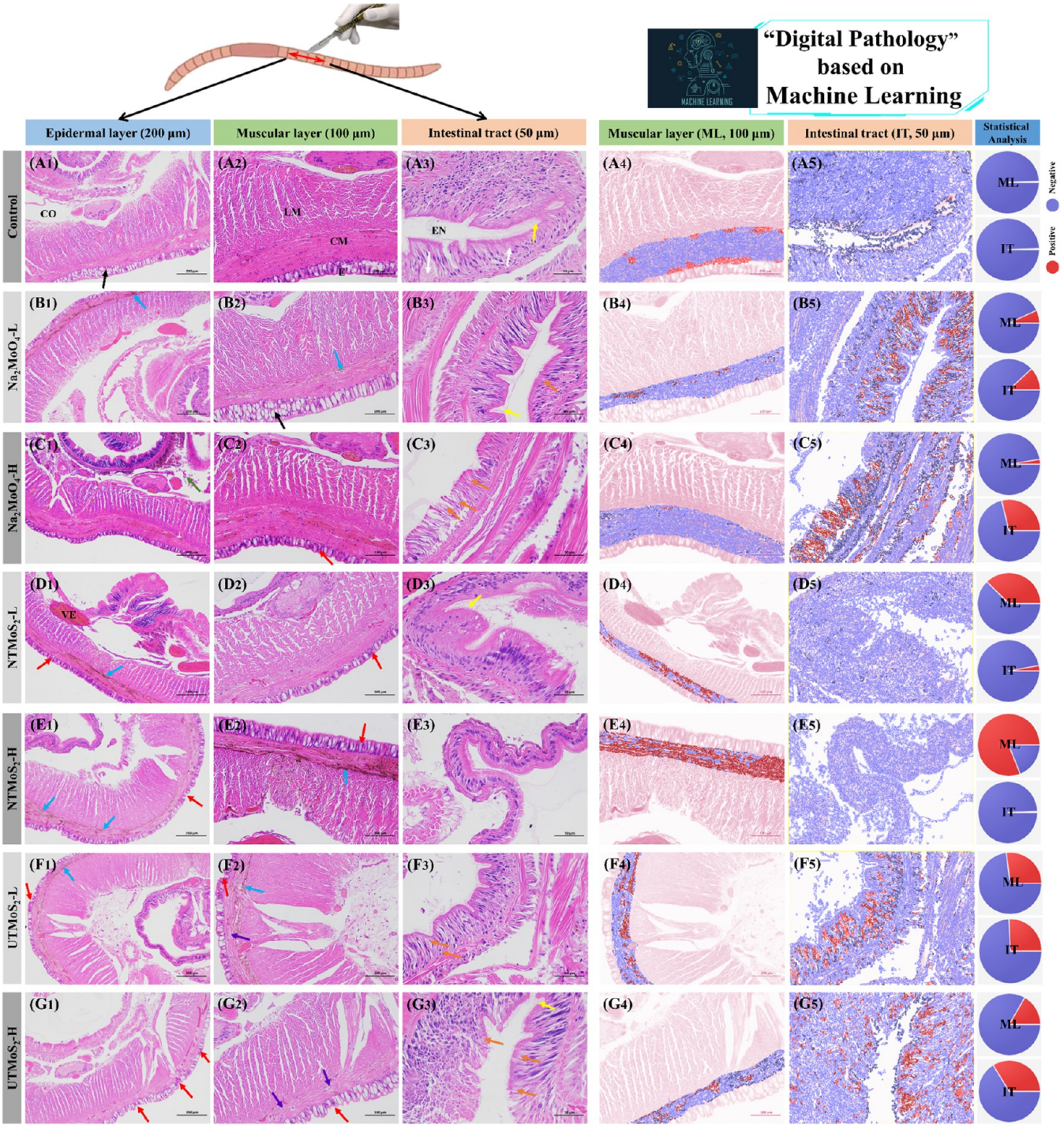

Figure 5. Hematoxylin−eosin (HE) staining and visual analysis based on machine learning in earthworms (*E. fetida*) following *in vivo* exposure for 96 h to different Mo forms (nontransformed ($NTMoS_2$) and UV-transformed ($UTMoS_2$) MoS_2 nanosheets and Na_2MoO_4). (A) Control; (B) Na_2MoO_4-L (10 mg Mo/L); (C) Na_2MoO_4-H (100 mg Mo/L); (D) $NTMoS_2$-L (10 mg Mo/L); (E) $NTMoS_2$-H (100 mg Mo/L); (F) $UTMoS_2$-L (10 mg Mo/L); and (G) $UTMoS_2$-H (100 mg Mo/L). Black arrows indicate abundant goblet cells. White arrows represent abundant fine secretory granules in the cytoplasm of epithelial cells. Yellow arrows denote visible microvilli on the surface of the intestine. Red arrows indicate reduced goblet cells or epidermal damage. Blue and purple arrows represent pathologic pigmentation and circular muscle breakage, respectively. Orange arrows indicate the fatty degeneration of intestinal mucosal epithelial cells and the formation of lipid vacuoles. Green arrows indicate the shedding of intestinal peripheral yellow cells. ML, muscular layer; IT, intestinal tract; CO, coelom; CM, circular muscle; LM, longitudinal muscle; EN, enterocoel; E, epithelium; VE, vessel.

respectively ($p < 0.01$, compared to control). Notably, the earthworm Mo content was significantly higher ($p < 0.01$) from Na_2MoO_4 than from $NTMoS_2$ and $UTMoS_2$ at the high dose. It has been reported that earthworms can rapidly accumulate ionic Mo with uptake rate constants ranging from 0.05 to 1.70 g soil g^{-1} worm d^{-1} (d.w.).[63] Similarly, Baccaro et al. observed that earthworms exhibited a significantly higher absorption of silver ion species compared to that of silver

https://doi.org/10.1021/acs.est.3c02518
Environ. Sci. Technol. 2023, 57, 11009−11021

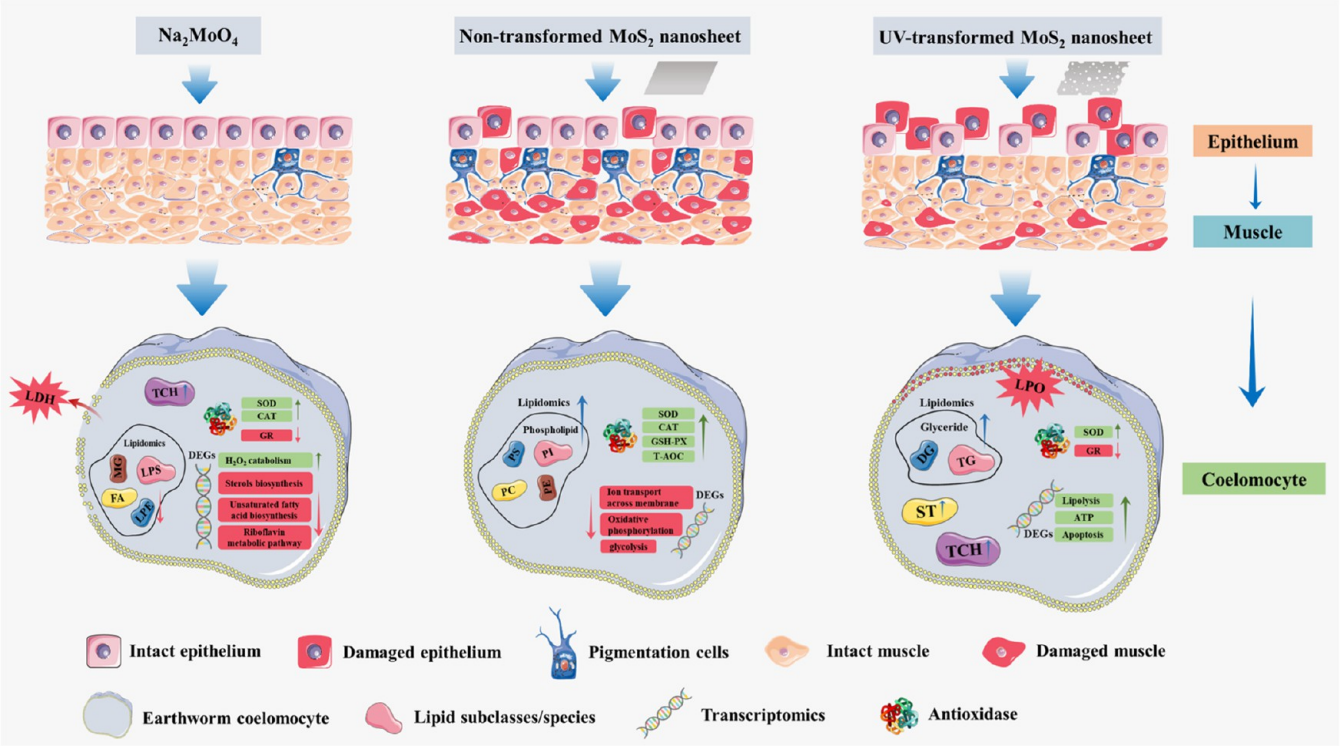

Figure 6. Schematic illustration of differential adverse outcome pathways (AOPs) associated with tissue, cellular, and molecular effects of nontransformed and UV-transformed MoS_2 nanosheets and Na_2MoO_4 on soil sentinel earthworm (*E. fetida*).

nanomaterials.[64] In the present study, we further distinguished the specific proportions of ionic Mo from the total Mo content accumulated in earthworms (Figure S21B). Due to the higher Mo ion release from $UTMoS_2$ (Figure S7A), the proportion of ionic Mo in earthworm total Mo accumulation of the $UTMoS_2$ group was significantly higher than that of the $NTMoS_2$ group at both exposure concentrations (Figure S21B; $p < 0.01$). Compared to MoS_2 nanosheets, the ionic counterpart can readily infiltrate and may exert different toxicity profiles from organism tissue to cell.[26,65] Considering the obvious alteration of the MoS_2 nanosheet morphology and different uptake patterns of Mo as a function of chemical form, image-based machine learning was further applied to investigate liposome damage upon different Mo forms of accumulation at the tissue level.

Image-Based Machine Learning Probes Liposome Damage at the Tissue Level. Compared to the control (Figure 5A_1−A_5), Na_2MoO_4 at 10 mg Mo/L caused slight circular muscle pigmentation and intestinal mucosal epithelium steatosis without destroying earthworm epithelial integrity (Figure 5B,C). The visualized analysis based on machine learning showed that earthworm intestinal damage was more significant upon Na_2MoO_4 exposure at 100 mg Mo/L, including the shedding of intestinal peripheral yellow cells (green arrow) and increasing lipid vacuolization (orange and red marks). The significant intestinal pathological damage is consistent with the high uptake pattern of Mo ions by the earthworms (Figure S21).

Two types of MoS_2 nanosheets at both doses caused varying degrees of epidermal and muscle stress, including epithelial layer contraction and goblet cell reduction (Figure 5D−G). Earthworms showed reduced epithelial thickness through the atrophy of goblet cells and increased body surface humidity favoring enhanced respiration under MoS_2 nanosheet stress, which could increase the risk of exposure and uptake of other xenobiotics.[66] Interestingly, although there was no difference in the total Mo uptake from the two types of MoS_2 nanosheets, machine learning identified that $NTMoS_2$ induced more pronounced circular muscle pigmentation in a concentration-dependent manner than $UTMoS_2$ (Figures S21 and 5D_4,E_4). Nevertheless, $NTMoS_2$ did not cause significant intestinal pathology regardless of the dose.

Earthworm epithelium integrity was disrupted (red arrows) upon 10 mg Mo/L of $UTMoS_2$ exposure. Circular muscle pigmentation (blue arrows) and intestinal lipid vacuoles were also observed (Figure 5F_1−F_3). The earthworm epithelium is the primary barrier against environmental stress.[67] Loss of earthworm epithelial integrity may lead to a higher exposure risk for the subepidermal muscle and intestinal tract.[56] This hypothesis was confirmed by the high-concentration groups. $UTMoS_2$ at 100 mg Mo/L resulted in more significant damage to the earthworm epithelium (Figure 5G_1, red arrows). Compared to $NTMoS_2$, highly transformed nanosheets are more likely to break and generate more sharp edges, which pose a significant risk to the epithelium during direct interaction or uptake by earthworms. Steatosis of earthworm intestinal mucosal epithelial cells was evident upon $UTMoS_2$ exposure at both doses (orange arrows in Figure 5F_3,G_3). Visual analysis of machine learning results showed that the intestinal lesion area was significantly larger for $UTMoS_2$- than for $NTMoS_2$-exposed groups (Figure 5F_5,G_5). Nanopores afford potentially active sites that contribute to enhanced electron transport during nanomaterial−cell interactions.[27] The boosted electron transport may damage biofilms and cause cellular degeneration. Additionally, considering the similar intestinal lipid degeneration in the Na_2MoO_4 groups, a higher Mo ion release related to the nanopore structure, and

https://doi.org/10.1021/acs.est.3c02518
Environ. Sci. Technol. 2023, 57, 11009−11021

the significant ionic accumulation by earthworms, the "ionic risk" from UTMoS$_2$ warrants further study.

Environmental Implications. The versatile applications of the MoS$_2$ nanosheet need to be carefully evaluated against associated environmental risks. The biocomplexity of liposomes and the application of sensitive mass spectrometry techniques provide important additional opportunities to expand the mechanistic understanding of such risks.[22,40,68] Within an *E. fetida* coelomocyte-based *in vivo* exposure strategy, the differential AOPs from exposure to MoS$_2$ nanosheets (non- and UV-transformed) and their ionic counterpart were distinguished using nontargeted lipidomics integrated with transcriptomics (Figure 6). Conventional Mo ion exposure primarily inhibited the *de novo* synthesis of key lipids (LPS, LPE, and FA) associated with membrane structure. Unlike the negative effects of Mo ions on membrane homeostasis, NTMoS$_2$ upregulated phospholipid (PS, PI, PE, and PC) contents, which may contribute to cell membrane structure remodeling. UTMoS$_2$ can specifically activate metabolic levels of ST (energy homeostasis) and glyceride (mediated lipid peroxidation), suggesting a cellular response to energy deprivation and oxidative stress. The advantage of coelomocyte lipid profiling following exposure to different Mo forms is that these liposomes are involved in a broad range of biological functions, thus helping us to identify novel AOPs in an unbiased manner. Using high-resolution LC-MS/MS, we can also identify additional structural features (e.g., carbon chain length, unsaturated bond numbers, etc.) within individual lipid species. However, in the framework of lipidomics-based ecological risk assessment, there is also a need to establish the link between captured liposomes and molecular endpoints and, ultimately, to determine the correlation with whole organism-level effects.[14,69] In the present study, transcriptomics and multiple phenotypic responses, including redox homeostasis, lipid peroxidation, and pathological damage, were used to validate the liposomal disorders detected at different levels of biological organization. Given these findings, future strategies for soil risk assessment should be further optimized, including the development of new biomarkers for AOPs by allowing functional identification from lipid subclasses to single species and the eventual expansion of liposome analysis to environmental monitoring.

■ ASSOCIATED CONTENT

Supporting Information

The Supporting Information is available free of charge at https://pubs.acs.org/doi/10.1021/acs.est.3c02518.

> Tested organisms and reagents, procedures for screening exposure concentrations, synthesis and characterization methods of MoS$_2$ nanosheets, coelomocyte isolation, LC-MS/MS and lipid search processes, RNA sequencing methods, digital pathology algorithm, tissue Mo content quantification, statistical analysis, TEM images, hydrodynamic diameters, infrared spectra, BET analysis, Raman spectra, surface roughness, Mo/S dissolution of MoS$_2$ nanosheets, lipidomics quality control, liposome composition and contents, lipid unsaturation degree and carbon chain length, PLS-DA and HCL analysis for lipidomics and transcriptomics, gene Venn maps and volcano diagrams, and gene KEGG enrichment and WGCNA analysis (PDF)

■ AUTHOR INFORMATION

Corresponding Authors

Hao Qiu − *School of Environmental Science and Engineering, Shanghai Jiao Tong University, Shanghai 200240, China;* orcid.org/0000-0002-4743-9702; Email: haoqiu@sjtu.edu.cn

Erkai He − *School of Geographic Sciences, East China Normal University, Shanghai 200241, China;* orcid.org/0000-0002-4866-3001; Email: ekhe@geo.ecnu.edu.cn

Authors

Kailun Sun − *School of Environmental Science and Engineering, Shanghai Jiao Tong University, Shanghai 200240, China*

Jason C. White − *The Connecticut Agricultural Experiment Station, New Haven, Connecticut 06504, United States;* orcid.org/0000-0001-5001-8143

Cornelis A. M. van Gestel − *Amsterdam Institute for Life and Environment (A-LIFE), Faculty of Science, Vrije Universiteit, Amsterdam 1081 HV, The Netherlands;* orcid.org/0000-0002-5651-0208

Willie J. G. M. Peijnenburg − *Center for the Safety of Substances and Products, National Institute of Public Health and the Environment, Bilthoven 3720 BA, The Netherlands; Institute of Environmental Sciences, Leiden University, Leiden 2300 RA, The Netherlands;* orcid.org/0000-0003-2958-9149

Complete contact information is available at: https://pubs.acs.org/10.1021/acs.est.3c02518

Notes

The authors declare no competing financial interest.

■ ACKNOWLEDGMENTS

The authors thank the National Natural Science Foundation of China (No. 42022057, No. 41977115, and No. 42277117) for financial support.

■ REFERENCES

(1) Zhang, X.; Grajal, J.; Vazquez-Roy, J. L.; Radhakrishna, U.; Wang, X.; Chern, W.; Zhou, L.; Lin, Y.; Shen, P.-C.; Ji, X.; Ling, X.; Zubair, A.; Zhang, Y.; Wang, H.; Dubey, M.; Kong, J.; Dresselhaus, M.; Palacios, T. Two-Dimensional MoS$_2$-Enabled Flexible Rectenna for Wi-Fi-Band Wireless Energy Harvesting. *Nature* **2019**, *566*, 368−372.

(2) Yadav, V.; Roy, S.; Singh, P.; Khan, Z.; Jaiswal, A. 2D MoS$_2$-Based Nanomaterials for Therapeutic, Bioimaging, and Biosensing Applications. *Small* **2019**, *15*, No. 1803706.

(3) Chen, S.; Shi, N.; Huang, M.; Tan, X.; Yan, X.; Wang, A.; Huang, Y.; Ji, R.; Zhou, D.; Zhu, Y.-G.; Keller, A. A.; Gardea-Torresdey, J. L.; White, J. C.; Zhao, L. MoS$_2$ Nanosheets−Cyanobacteria Interaction: Reprogrammed Carbon and Nitrogen Metabolism. *ACS Nano* **2021**, *15*, 16344−16356.

(4) Wang, Z.; Mi, B. Environmental Applications of 2D Molybdenum Disulfide (MoS$_2$) Nanosheets. *Environ. Sci. Technol.* **2017**, *51*, 8229−8244.

(5) Zeng, H.; Hu, X.; Zhou, Q.; Luo, J.; Hou, X. Extracellular Polymeric Substances Mediate Defect Generation and Phytotoxicity of Single-Layer MoS$_2$. *J. Hazard. Mater.* **2022**, *429*, No. 128361.

(6) Zou, W.; Li, X.; Li, C.; Sun, Y.; Zhang, X.; Jin, C.; Jiang, K.; Zhou, Q.; Hu, X. Influence of Size and Phase on the Biodegradation, Excretion, and Phytotoxicity Persistence of Single-Layer Molybdenum Disulfide. *Environ. Sci. Technol.* **2020**, *54*, 12295−12306.

(7) Liu, S.; Shen, Z.; Wu, B.; Yu, Y.; Hou, H.; Zhang, X.-X.; Ren, H. Cytotoxicity and Efflux Pump Inhibition Induced by Molybdenum

Disulfide and Boron Nitride Nanomaterials with Sheetlike Structure. *Environ. Sci. Technol.* **2017**, *51*, 10834−10842.
(8) Chng, E. L. K.; Sofer, Z.; Pumera, M. MoS_2 Exhibits Stronger Toxicity with Increased Exfoliation. *Nanoscale* **2014**, *6*, 14412−14418.
(9) Li, W.; Zhang, P.; Qiu, H.; Van Gestel, C. A. M.; Peijnenburg, W. J. G. M.; Cao, X.; Zhao, L.; Xu, X.; He, E. Commonwealth of Soil Health: How Do Earthworms Modify the Soil Microbial Responses to CeO_2 Nanoparticles? *Environ. Sci. Technol.* **2022**, *56*, 1138−1148.
(10) Yang, Y.; Xiao, Y.; Li, M.; Ji, F.; Hu, C.; Cui, Y. Evaluation of Complex Toxicity of Canbon Nanotubes and Sodium Pentachlorophenol Based on Earthworm Coelomocytes Test. *PLoS One* **2017**, *12*, No. e170092.
(11) Garcia-Velasco, N.; Irizar, A.; Urionabarrenetxea, E.; Scott-Fordsmand, J. J.; Soto, M. Selection of an Optimal Culture Medium and the Most Responsive Viability Assay to Assess AgNPs Toxicity with Primary Cultures of *Eisenia fetida* Coelomocytes. *Ecotoxicol. Environ. Saf.* **2019**, *183*, No. 109545.
(12) Xu, K.; Wang, X.; Lu, C.; Liu, Y.; Zhang, D.; Cheng, J. Toxicity of Three Carbon-Based Nanomaterials to Earthworms: Effect of Morphology on Biomarkers, Cytotoxicity, and Metabolomics. *Sci. Total Environ.* **2021**, *777*, No. 146224.
(13) Xu, K.; Liu, Y.-X.; Wang, X.-F.; Li, S.-W.; Cheng, J.-M. Combined Toxicity of Functionalized Nano-Carbon Black and Cadmium on *Eisenia fetida* Coelomocytes: The Role of Adsorption. *J. Hazard. Mater.* **2020**, *398*, No. 122815.
(14) Zhen, H.; Teng, Q.; Mosley, J. D.; Collette, T. W.; Yue, Y.; Bradley, P. M.; Ekman, D. R. Untargeted Lipidomics for Determining Cellular and Subcellular Responses in Zebrafish (*Danio rerio*) Liver Cells Following Exposure to Complex Mixtures in U.S. Streams. *Environ. Sci. Technol.* **2021**, *55*, 8180−8190.
(15) Moreau, A.; Téruel, C.; Beylot, M.; Albalea, V.; Tamasi, V.; Umbdenstock, T.; Parmentier, Y.; Sa-Cunha, A.; Suc, B.; Fabre, J.-M.; Navarro, F.; Ramos, J.; Meyer, U.; Maurel, P.; Vilarem, M.-J.; Pascussi, J.-M. A Novel Pregnane X Receptor and S14-Mediated Lipogenic Pathway in Human Hepatocyte. *Hepatology* **2009**, *49*, 2068−2079.
(16) Sun, Z.; Tang, Z.; Yang, X.; Liu, Q. S.; Zhang, J.; Zhou, Q.; Jiang, G. 3-Tert-Butyl-4-Hydroxyanisole Impairs Hepatic Lipid Metabolism in Male Mice Fed with a High-Fat Diet. *Environ. Sci. Technol.* **2022**, *56*, 3204−3213.
(17) He, Z.; Zhang, H.; Song, Y.; Yang, Z.; Cai, Z. Exposure to Ambient Fine Particulate Matter Impedes the Function of Spleen in the Mouse Metabolism of High-Fat Diet. *J. Hazard. Mater.* **2022**, *423*, No. 127129.
(18) Zhang, W.; Huo, T.; Li, A.; Wu, X.; Feng, C.; Liu, J.; Jiang, H. Identification of Neurotoxicity Markers Induced by Realgar Exposure in the Mouse Cerebral Cortex Using Lipidomics. *J. Hazard. Mater.* **2020**, *389*, No. 121567.
(19) Huang, W.; Xie, P.; Cai, Z. Lipid Metabolism Disorders Contribute to Hepatotoxicity of Triclosan in Mice. *J. Hazard. Mater.* **2020**, *384*, No. 121310.
(20) Wei, J.; Li, X.; Xiang, L.; Song, Y.; Liu, Y.; Jiang, Y.; Cai, Z. Metabolomics and Lipidomics Study Unveils the Impact of Polybrominated Diphenyl Ether-47 on Breast Cancer Mice. *J. Hazard. Mater.* **2020**, *390*, No. 121451.
(21) Ji, F.; Sreenivasmurthy, S. G.; Wei, J.; Shao, X.; Luan, H.; Zhu, L.; Song, J.; Liu, L.; Li, M.; Cai, Z. Study of BDE-47 Induced Parkinson's Disease-like Metabolic Changes in C57BL/6 Mice by Integrated Metabolomic, Lipidomic and Proteomic Analysis. *J. Hazard. Mater.* **2019**, *378*, No. 120738.
(22) Marqueño, A.; Blanco, M.; Maceda-Veiga, A.; Porte, C. Skeletal Muscle Lipidomics as a New Tool to Determine Altered Lipid Homeostasis in Fish Exposed to Urban and Industrial Wastewaters. *Environ. Sci. Technol.* **2019**, *53*, 8416−8425.
(23) Lee, T.-W.; Chen, C.-C.; Chen, C. Chemical Stability and Transformation of Molybdenum Disulfide Nanosheets in Environmental Media. *Environ. Sci. Technol.* **2019**, *53*, 6282−6291.
(24) Zou, W.; Zhou, Q.; Zhang, X.; Hu, X. Environmental Transformations and Algal Toxicity of Single-Layer Molybdenum Disulfide Regulated by Humic Acid. *Environ. Sci. Technol.* **2018**, *52*, 2638−2648.
(25) Zou, W.; Zhou, Q.; Zhang, X.; Hu, X. Dissolved Oxygen and Visible Light Irradiation Drive the Structural Alterations and Phytotoxicity Mitigation of Single-Layer Molybdenum Disulfide. *Environ. Sci. Technol.* **2019**, *53*, 7759−7769.
(26) Wang, Z.; von dem Bussche, A.; Qiu, Y.; Valentin, T. M.; Gion, K.; Kane, A. B.; Hurt, R. H. Chemical Dissolution Pathways of MoS_2 Nanosheets in Biological and Environmental Media. *Environ. Sci. Technol.* **2016**, *50*, 7208−7217.
(27) Shi, T.; Hou, X.; Guo, S.; Zhang, L.; Wei, C.; Peng, T.; Hu, X. Nanohole-Boosted Electron Transport between Nanomaterials and Bacteria as a Concept for Nano−Bio Interactions. *Nat. Commun.* **2021**, *12*, No. 493.
(28) Zeng, H.; Hu, X.; Ouyang, S.; Zhou, Q. Nanocolloids, but Not Humic Acids, Augment the Phytotoxicity of Single-Layer Molybdenum Disulfide Nanosheets. *Environ. Sci. Technol.* **2021**, *55*, 1122−1133.
(29) Cao, X.; Gan, X.; Lang, H.; Peng, Y. Impact of the Surface and Microstructure on the Lubricative Properties of MoS_2 Aging under Different Environments. *Langmuir* **2021**, *37*, 2928−2941.
(30) Organization for Economic Co-operation and Development (OECD). *Guidelines for the Testing of Chemicals, No. 222: Earthworm Reproduction Test (Eisenia fetida/Eisenia andrei)*, 2006.
(31) International Organization for Standards (ISO). *Soil Quality-Effects of Pollutants on Earthworms-Determination of Effects on Reproduction of Eisenia fetida/Eisenia andrei (Endorsed by AENOR in September of 2015)*, 2015.
(32) Eyambe, G. S.; Goven, A. J.; Fitzpatrick, L. C.; Venables, B. J.; Cooper, E. L. A Non-Invasive Technique for Sequential Collection of Earthworm (*Lumbricus terrestris*) Leukocytes during Subchronic Immunotoxicity Studies. *Lab. Anim.* **1991**, *25*, 61−67.
(33) Bankhead, P.; Loughrey, M. B.; Fernández, J. A.; Dombrowski, Y.; McArt, D. G.; Dunne, P. D.; McQuaid, S.; Gray, R. T.; Murray, L. J.; Coleman, H. G.; James, J. A.; Salto-Tellez, M.; Hamilton, P. W. QuPath: Open Source Software for Digital Pathology Image Analysis. *Sci. Rep.* **2017**, *7*, No. 16878.
(34) Qiu, H.; He, E. Development of Electrostatic-Based Bioavailability Models for Interpreting and Predicting Differential Phytotoxicity and Uptake of Metal Mixtures across Different Soils. *Environ. Pollut.* **2017**, *226*, 308−316.
(35) Cançado, L. G.; Jorio, A.; Ferreira, E. H. M.; Stavale, F.; Achete, C. A.; Capaz, R. B.; Moutinho, M. V. O.; Lombardo, A.; Kulmala, T. S.; Ferrari, A. C. Quantifying Defects in Graphene via Raman Spectroscopy at Different Excitation Energies. *Nano Lett.* **2011**, *11*, 3190−3196.
(36) Lee, C.; Yan, H.; Brus, L. E.; Heinz, T. F.; Hone, J.; Ryu, S. Anomalous Lattice Vibrations of Single- and Few-Layer MoS_2. *ACS Nano* **2010**, *4*, 2695−2700.
(37) George, S.; Lin, S.; Ji, Z.; Thomas, C. R.; Li, L.; Mecklenburg, M.; Meng, H.; Wang, X.; Zhang, H.; Xia, T.; Hohman, J. N.; Lin, S.; Zink, J. I.; Weiss, P. S.; Nel, A. E. Surface Defects on Plate-Shaped Silver Nanoparticles Contribute to Its Hazard Potential in a Fish Gill Cell Line and Zebrafish Embryos. *ACS Nano* **2012**, *6*, 3745−3759.
(38) Nel, A. E.; Mädler, L.; Velegol, D.; Xia, T.; Hoek, E. M. V.; Somasundaran, P.; Klaessig, F.; Castranova, V.; Thompson, M. Understanding Biophysicochemical Interactions at the Nano−Bio Interface. *Nat. Mater.* **2009**, *8*, 543−557.
(39) Xie, J.; Zhang, H.; Li, S.; Wang, R.; Sun, X.; Zhou, M.; Zhou, J.; Lou, X. W.; Xie, Y. Defect-Rich MoS_2 Ultrathin Nanosheets with Additional Active Edge Sites for Enhanced Electrocatalytic Hydrogen Evolution. *Adv. Mater.* **2013**, *25*, 5807−5813.
(40) Marqueño, A.; Flores, C.; Casado, M.; Porte, C. Dysregulation of Lipid Metabolism in PLHC-1 and ZFL Cells Exposed to Tributyltin an All-Trans Retinoic Acid. *Aquat. Toxicol.* **2021**, *231*, No. 105733.
(41) van Meer, G.; Voelker, D. R.; Feigenson, G. W. Membrane Lipids: Where They Are and How They Behave. *Nat. Rev. Mol. Cell Biol.* **2008**, *9*, 112−124.

(42) Han, X. Lipidomics for Studying Metabolism. *Nat. Rev. Endocrinol.* **2016**, *12*, 668−679.
(43) Rodriguez-Cuenca, S.; Pellegrinelli, V.; Campbell, M.; Oresic, M.; Vidal-Puig, A. Sphingolipids and Glycerophospholipids − The "Ying and Yang" of Lipotoxicity in Metabolic Diseases. *Prog. Lipid Res.* **2017**, *66*, 14−29.
(44) Zhang, J.; Liang, S.; Ning, R.; Jiang, J.; Zhang, J.; Shen, H.; Chen, R.; Duan, J.; Sun, Z. $PM_{2.5}$-Induced Inflammation and Lipidome Alteration Associated with the Development of Atherosclerosis Based on a Targeted Lipidomic Analysis. *Environ. Int.* **2020**, *136*, No. 105444.
(45) Chen, W.-L.; Lin, C.-Y.; Yan, Y.-H.; Cheng, K. T.; Cheng, T.-J. Alterations in Rat Pulmonary Phosphatidylcholines after Chronic Exposure to Ambient Fine Particulate Matter. *Mol. BioSyst.* **2014**, *10*, 3163−3169.
(46) Li, T.; Yin, Y.; Zhou, Z.; Qiu, J.; Liu, W.; Zhang, X.; He, K.; Cai, Y.; Zhu, Z.-J. Ion Mobility-Based Sterolomics Reveals Spatially and Temporally Distinctive Sterol Lipids in the Mouse Brain. *Nat. Commun.* **2021**, *12*, No. 4343.
(47) Mosegaard, S.; Dipace, G.; Bross, P.; Carlsen, J.; Gregersen, N.; Olsen, R. K. J. Riboflavin Deficiency—Implications for General Human Health and Inborn Errors of Metabolism. *Int. J. Mol. Sci.* **2020**, *21*, 3847.
(48) Weidemüller, P.; Kholmatov, M.; Petsalaki, E.; Zaugg, J. B. Transcription Factors: Bridge between Cell Signaling and Gene Regulation. *Proteomics* **2021**, *21*, No. e2000034.
(49) Hermansson, M.; Hokynar, K.; Somerharju, P. Mechanisms of Glycerophospholipid Homeostasis in Mammalian Cells. *Prog. Lipid Res.* **2011**, *50*, 240−257.
(50) Wang, X.; Qin, Y.; Li, X.; Yan, B.; Martyniuk, C. J. Comprehensive Interrogation of Metabolic and Bioenergetic Responses of Early-Staged Zebrafish (*Danio rerio*) to a Commercial Copper Hydroxide Nanopesticide. *Environ. Sci. Technol.* **2021**, *55*, 13033−13044.
(51) McCommis, K. S.; Finck, B. N. Mitochondrial Pyruvate Transport: A Historical Perspective and Future Research Directions. *Biochem. J.* **2015**, *466*, 443−454.
(52) Poulaki, A.; Giannouli, S. Mitochondrial Lipids: From Membrane Organization to Apoptotic Facilitation. *Int. J. Mol. Sci.* **2022**, *23*, 3738.
(53) Shanta, P. V.; Li, B.; Stuart, D. D.; Cheng, Q. Lipidomic Profiling of Algae with Microarray MALDI-MS toward Ecotoxicological Monitoring of Herbicide Exposure. *Environ. Sci. Technol.* **2021**, *55*, 10558−10568.
(54) Fukawa, T.; Yan-Jiang, B. C.; Min-Wen, J. C.; Jun-Hao, E. T.; Huang, D.; Qian, C.-N.; Ong, P.; Li, Z.; Chen, S.; Mak, S. Y.; Lim, W. J.; Kanayama, H.; Mohan, R. E.; Wang, R. R.; Lai, J. H.; Chua, C.; Ong, H. S.; Tan, K.-K.; Ho, Y. S.; Tan, I. B.; Teh, B. T.; Shyh-Chang, N. Excessive Fatty Acid Oxidation Induces Muscle Atrophy in Cancer Cachexia. *Nat. Med.* **2016**, *22*, 666−671.
(55) Lenton, L. M.; Behm, C. A.; Bygrave, F. L. Aberrant Mitochondrial Respiration in the Livers of Rats Infected with Fasciola Hepatica: The Role of Elevated Non-Esterified Fatty Acids and Altered Phospholipid Composition. *Biochem. J* **1995**, *307*, 425−431.
(56) Sun, K.; Li, M.; Song, Y.; Tang, J.; Liu, R. Organism and Molecular-Level Responses of Superoxide Dismutase Interaction with 2-Pentanone. *Chemosphere* **2021**, *286*, No. 131707.
(57) Ahmad, R.; Tripathi, A. K.; Tripathi, P.; Singh, S.; Singh, R.; Singh, R. K. Malondialdehyde and Protein Carbonyl as Biomarkers for Oxidative Stress and Disease Progression in Patients with Chronic Myeloid Leukemia. *In Vivo* **2008**, *22*, 525−528.
(58) Livingstone, D. R. Contaminant-Stimulated Reactive Oxygen Species Production and Oxidative Damage in Aquatic Organisms. *Mar. Pollut. Bull.* **2001**, *42*, 656−666.
(59) Antunes, F.; Han, D.; Cadenas, E. Relative Contributions of Heart Mitochondria Glutathione Peroxidase and Catalase to H_2O_2 Detoxification in *in Vivo* Conditions. *Free Radical Biol. Med.* **2002**, *33*, 1260−1267.
(60) Sun, K.; Song, Y.; Liu, Z.; Jing, M.; Wan, J.; Tang, J.; Liu, R. Toxicity Assessment of Fluoranthene, Benz(a)Anthracene and Its Mixed Pollution in Soil: Studies at the Molecular and Animal Levels. *Ecotoxicol. Environ. Saf.* **2020**, *202*, No. 110864.
(61) Al-Othman, A. M.; Al-Numair, K. S.; El-Desoky, G. E.; Yusuf, K.; Al Othman, Z. A.; Aboul-Soud, M. A. M.; Giesy, J. P. Protection of Alpha-Tocopherol and Selenium against Acute Effects of Malathion on Liver and Kidney of Rats. *Afr. J. Pharm. Pharmacol.* **2011**, *5*, 1263−1271.
(62) Weydert, C. J.; Cullen, J. J. Measurement of Superoxide Dismutase, Catalase and Glutathione Peroxidase in Cultured Cells and Tissue. *Nat. Protoc.* **2010**, *5*, 51−66.
(63) Díez-Ortiz, M.; Giska, I.; Groot, M.; Borgman, E. M.; Van Gestel, C. A. M. Influence of Soil Properties on Molybdenum Uptake and Elimination Kinetics in the Earthworm *Eisenia andrei*. *Chemosphere* **2010**, *80*, 1036−1043.
(64) Baccaro, M.; Undas, A. K.; de Vriendt, J.; van den Berg, J. H. J.; Peters, R. J. B.; van den Brink, N. W. Ageing, Dissolution and Biogenic Formation of Nanoparticles: How Do These Factors Affect the Uptake Kinetics of Silver Nanoparticles in Earthworms. *Environ. Sci.: Nano* **2018**, *5*, 1107−1116.
(65) Stafford, J. M.; Lambert, C. E.; Zyskowski, J. A.; Engfehr, C. L.; Fletcher, O. J.; Clark, S. L.; Tiwary, A.; Gulde, C. M.; Sample, B. E. Dietary Toxicity of Soluble and Insoluble Molybdenum to Northern Bobwhite Quail (*Colinus virginianus*). *Ecotoxicology* **2016**, *25*, 291−301.
(66) Cunha, L.; Campos, I.; Montiel, R.; Rodrigues, A.; Morgan, A. J. Morphometry of the Epidermis of an Invasive Megascoelecid Earthworm (*Amynthas gracilis*, Kinberg 1867) Inhabiting Actively Volcanic Soils in the Azores Archipelago. *Ecotoxicol. Environ. Saf.* **2011**, *74*, 25−32.
(67) Zhang, W.; Liu, K.; Li, J.; Liang, J.; Lin, K. Impacts of BDE209 Addition on Pb Uptake, Subcellular Partitioning and Gene Toxicity in Earthworm (*Eisenia fetida*). *J. Hazard. Mater.* **2015**, *300*, 737−744.
(68) Dreier, D. A.; Nouri, M.-Z.; Denslow, N. D.; Martyniuk, C. J. Lipidomics Reveals Multiple Stressor Effects (Temperature × Mitochondrial Toxicant) in the Zebrafish Embryo Toxicity Test. *Chemosphere* **2021**, *264*, No. 128472.
(69) Dreier, D. A.; Bowden, J. A.; Aristizabal-Henao, J. J.; Denslow, N. D.; Martyniuk, C. J. Ecotoxico-Lipidomics: An Emerging Concept to Understand Chemical-Metabolic Relationships in Comparative Fish Models. *Comp. Biochem. Physiol., Part D* **2020**, *36*, No. 100742.

https://doi.org/10.1021/acs.est.3c02518
Environ. Sci. Technol. 2023, 57, 11009−11021